Author Manuscript

Author Manuscript

Author Manuscript

Author Manuscript

HHS Public Access

Author manuscript

NMR Biomed. Author manuscript; available in PMC 2018 March 01.

Published in final edited form as:

NMR Biomed. 2017 March ; 30(3): . doi:10.1002/nbm.3563.

Skeletal Muscle DT-MRI Fiber Tracking: Rationale, Data Acquisition and Analysis Methods, Applications, and Future Directions

Bruce M. Damon[1,2,3,4], **Martijn Froeling**[5], **Amanda K. W. Buck**[1,2,3], **Jos Oudeman**[6], **Zhaohua Ding**[1,2,3,7], **Aart J. Nederveen**[6], **Emily C. Bush**[1], and **Gustav J. Strijkers**[8]

[1]Institute of Imaging Science, Vanderbilt University, Nashville TN USA [2]Department of Radiology and Radiological Sciences, Vanderbilt University, Nashville TN USA [3]Department of Biomedical Engineering, Vanderbilt University, Nashville TN USA [4]Department of Molecular Physiology and Biophysics, Vanderbilt University, Nashville TN USA [5]Department of Radiology, University Medical Center, Utrecht, the Netherlands [6]Department of Radiology, Academic Medical Center, Amsterdam, the Netherlands [7]Department of Electrical Engineering and Computer Engineering, Vanderbilt University, Nashville TN USA [8]Department of Biomedical Engineering and Physics, Academic Medical Center, Amsterdam, the Netherlands

Abstract

The mechanical functions of muscles are generating force and actuating movement by shortening or lengthening under load. These functions are influenced, in part, by the internal arrangement of muscle fibers with respect to the muscle's mechanical line of action. This property is known as muscle architecture. In this review, we describe the use of diffusion-tensor (DT-) MRI muscle fiber tracking for studying muscle architecture. In the first section, the importance of skeletal muscle architecture to function is discussed. Also, traditional and complementary methods for assessing muscle architecture (brightness-mode ultrasound imaging and cadaver analysis) are presented. Next, DT-MRI is introduced and the structural basis for the reduced and anisotropic diffusion of water in muscle is discussed. The third section discusses issues related to the acquisition of skeletal muscle DT-MRI data and presents recommendations for optimal strategies. The fourth section discusses methods for pre-processing DT-MRI data, the available approaches for calculating the diffusion tensor and seeding and propagating fiber tracts, and analyzing the tracking results to measure structural properties pertinent to muscle biomechanics. Lastly, examples of how DT-MRI fiber tracking has been used to provide new insights into how muscle function are presented and important future research directions are highlighted.

Keywords

Muscle architecture; diffusion MRI; skeletal muscle; muscle mechanics; non-invasive

Address for correspondence: Bruce M. Damon, PhD, Institute of Imaging Science, Vanderbilt University, AA-1105 MCN, 1161 21st Ave S, Nashville, TN USA, Ph. (615) 322-8355, Fax: (615) 322-0734, bruce.damon@vanderbilt.edu.

Author Manuscript Author Manuscript Author Manuscript Author Manuscript

PURPOSE AND SCOPE OF THIS REVIEW

Skeletal muscles serve critical mechanical and physiological roles in the body. The mechanical functions include generating force and actuating movement by shortening or lengthening under load. Although these properties are affected primarily by the rate at which the muscle contractile protein complex can hydrolyze ATP during the cross-bridge cycle, it transpires that a muscle's abilities to generate force or undergo large and/or rapid length excursions are also influenced by the internal arrangement of muscle fibers with respect to the muscle's mechanical line of action. This property is commonly known as muscle architecture. Our aim in this review is to describe the use of diffusion-tensor (DT-) MRI muscle fiber tracking for studying these structural properties. We will discuss the importance of muscle structure to muscle function and how muscle architecture is typically assessed; describe DT-MRI and its application to muscle; discuss issues and make recommendations for data acquisition and analysis; provide examples of how DT-MRI data have been used to provide new insights into how muscles function; and lastly, highlight important future research directions.

RATIONALE FOR STUDYING MUSCLE STRUCTURE USING DT-MRI

Skeletal Muscle Structure and Its Importance to Function

In this review, we consider the structural properties of skeletal muscle at three levels of biological organization: molecular-cellular, tissue-organ, and gross anatomical. At each of these levels, there are structural properties that influence a muscle's overall mechanical behavior. DT-MRI fiber tracking is used to study the tissue-organ scale structural features that impact muscle mechanical behavior. The ability of DT-MRI fiber tracking methods to quantify muscle architecture arises from certain molecular and cellular properties of muscle. Correspondingly, we consider molecular-cellular and tissue-organ scale properties in the greatest detail. As the assessment of gross anatomical properties does not require DT-MRI, we consider these issues just briefly.

The structural properties at the gross anatomical level relate primarily to a muscle's volume and location within the body. Muscles run from a point or region of origin (generally, located more proximally) to a point of insertion (generally, located more distally). In most cases, either the muscle or its tendon of insertion will cross a freely moving joint and connect to the skeleton in a more distal body segment. When such a muscle contracts, it generates a torque about that joint; typically, the body segment rotates. The type of anatomical movement (flexion, extension, *etc.*) depends on the anatomical relationship between the muscle's origin and insertion and the muscle's placement in the skeleton. The origin and insertion also define the muscle's mechanical line of action. Conventional structural MR imaging methods are often used to quantify structural properties at the gross anatomical level for use in studies of disease natural history or for inclusion in biomechanical models. We turn now to describe some of the cellular and molecular-scale properties of muscle.

Vertebrate skeletal muscle twitch-type fibers are multinucleated cells with an oblate polygonal cross section (1). In cross-section, their mean width is about 55 μm (range, ~20–

Author Manuscript Author Manuscript Author Manuscript Author Manuscript

90 μm) (2); in humans, they can be as long as 40 cm (3). Like other cells, they are bounded by a plasma membrane and a basement membrane. The plasma membrane has a permeability to water of about 13×10^{-4} cm/s (4). An extracellular matrix (ECM), composed of collagen fibers, other connective tissue proteins and glycoproteins, and ground substance, surrounds the basement membrane. When the muscle is at shortened or typical resting lengths, the collagen fibers of the ECM are arranged in random orientations; however, when a muscle lengthens, the collagen fibers rotate to lie approximately parallel to the muscle fibers (5).

Most of the intracellular space is occupied by the contractile protein arrays, called myofibrils, and the water within and around them. Myofibrils are composed of a series of repeating structures called sarcomeres. Sarcomeres are the smallest functional units of muscle contraction *in vivo*. Each sarcomere consists of inter-digitating protein filaments, referred to as the thick and thin filaments. At the ends, sarcomeres are defined by a structure called the Z-line. In cross-section, the protein filaments are spaced tens of nanometers apart, while the sarcomere length is typically 2–3 μm. An organelle called the sarcoplasmic reticulum (SR) surrounds the myofibrils. When Ca^{2+} is released from the SR, a molecular interaction between actin on the thin filament and myosin of the thick filament can occur. Protein connections between the myofibrils and the extracellular matrix serve as the modes of force transmission and provide structural integrity to the plasma membrane. These connections occur both at the ends of fibers and laterally. Either directly or indirectly, muscle fibers are connected to (insert into) a tendon or aponeurosis.

At the intermediate scale (between the individual fibers and the whole muscle), different muscles exhibit considerable muscle architectural variability. Full reviews of muscle architecture, the variety of architectural designs, and their functional implications have been presented elsewhere (6, 7); only a brief overview is provided here. The most basic distinction is between the fusiform and pennate architectural patterns. In a fusiform muscle, the fibers' longitudinal axes lie generally parallel to the muscle's line of action. Per unit volume, this architecture places more sarcomeres in series; when two sarcomeres arrayed in series contract, their displacements add. Consequently, fusiform architectures favor greater length excursions (8) and shortening velocities (9). The semitendinosus muscle is an example of a fusiform architectures (Fig. 1A). In pennate muscles, such as the gastrocnemius and soleus muscles (Fig. 1B), the fibers are arranged obliquely to the muscle's line of action. This architecture places more sarcomeres in parallel. When two sarcomeres in parallel contract simultaneously, their forces add; thus, pennate architectures tend to favor higher levels of force production. A simple estimate of the effect pennation on force production is obtained by calculating the physiological cross-sectional area (PCSA):

$$\mathrm{PCSA}=\frac{V_M}{L_f}\cdot\cos(\theta) \quad (1)$$

where V_M is the muscle volume, L_f is the fiber length, and θ is the pennation angle (defined as the angle formed by the local tangents to the muscle fibers and the tendon of insertion). Importantly, the PCSA is better correlated with peak isometric force production than is the

Author Manuscript Author Manuscript Author Manuscript Author Manuscript

anatomical cross-sectional area (10). Clearly, muscle architecture impacts a muscle's ability to perform its mechanical functions – generating force and actuating movement.

In addition to these basic architecture patterns and effects, other structural properties can also influence the characteristics of muscle contraction. One example is fiber curvature (κ). Because muscle volume decreases slightly during contraction, intramuscular fluid pressure increases during contraction (11, 12). Several theoretical works (13–15) have predicted that fiber curvature may create fluid pressure gradients between the concave and convex surfaces of the fiber; these gradients are further predicted to add as a function of muscle depth. Because these pressures can be high enough to occlude blood flow, these gradients may influence intramuscular perfusion patterns. Miura *et al.* provided data consistent with this prediction (16). Another important property is architectural heterogeneity. Many studies have reported intramuscular heterogeneity in strain development during contraction (17–21). These may be due to intramuscular heterogeneity in architectural patterns (22, 23). A major motivation for quantifying muscle architecture is to describe the underlying structural scaffold of the muscle, such that mechanical and physiological behaviors can be understood with respect to structure.

Traditional Approaches to Studying Skeletal Muscle Architecture

The original methods for studying muscle architecture used manual measurements in cadaver specimens. Data such as V_M, θ, and fiber or fascicle length were obtained. While subject to obvious limitations such as cadaver availability, the pre-mortem age and health status of the subjects, fixation artifacts, and a large investment of time, there are several distinct advantages of this approach. First, it allows comprehensive databases to be developed (3, 24). Also, it is the current best approach for comprehensively measuring sarcomere length (3), a critical determinant of the force potential of a muscle (25). Lastly, it allows higher order architectural patterns, such as the existence of series-fibered muscles, to be appreciated. Features such as sarcomere length and series fiber arrangements are below the contrast and/or resolution limits of non-invasive *in vivo* methods.

To measure tissue-organ scale muscle architectural properties *in vivo*, imaging approaches are typically used. Brightness-mode (B-mode) ultrasound (US) imaging has been used for this purpose for more than 20 years (26). Most of the more than 100 implementations of US imaging for muscle architecture measurements used two-dimensional (2-D) imaging methods (Fig. 2), with a few studies that used 3-D imaging (27–29). The high frame rates of US imaging lend this approach to studying dynamic events such as muscle contraction. Ultrasound has been used to measure L_f, κ, and θ in the resting and contracting states (*e.g.* (30–33)) and to measure strains in aponeuroses, tendons, and muscles during contraction (*e.g.* (34, 35)). A recent review of the use of US in studies of muscle architecture is by Cronin and Lichtwark (36).

Diffusion-Tensor MRI

General Principles—Diffusion-weighted MRI (DW-MRI) and DT-MRI have found application in studies of pathology (*e.g.*, stroke, myocardial damage, and skeletal muscle damage) and for microscopic tissue characterization. In addition, the coupling of the water

Author Manuscript Author Manuscript Author Manuscript Author Manuscript

diffusion profile with local tissue structure allows DT-MRI to probe tissue connectivity non-invasively, an approach commonly known as DT-MRI tracking (37). DW-MRI and DT-MRI have been reviewed extensively elsewhere (37–39); this review summarizes the fundamental aspects of these methods and discusses skeletal muscle-specific issues.

The Stejskal-Tanner pulsed-gradient spin-echo sequence (40) is the most commonly used pulse sequence for DW-MRI. It uses a pair of magnetic field gradients, placed symmetrically about the refocusing pulse, to encode diffusion. The first gradient application disperses the phases of the protons' magnetic moments, while the second gradient tends to restore phase coherence. If transverse relaxation processes are ignored, the protons' phase coherence is completely restored for stationary water molecules and incompletely restored for diffusing water molecules. The incomplete phase restoration for diffusing water molecules causes the MRI signal, S, to decay exponentially:

$$S - S_0 \cdot e^{-\mathrm{bD}} \quad (2)$$

where S_0 is the baseline MR signal, D is the scalar self-diffusion coefficient, and the b-factor characterizes the diffusion gradient pulses' duration, spacing, amplitude, and geometry. The measurement is sensitive only to diffusion in the direction of the gradient.

In general, the diffusion coefficient for water in tissues is lower than that for free water. This reduction in D occurs because, on the time scale of the diffusion-encoding process, structures such as protein filaments and cell membranes tend to hinder water diffusion. When DW-MRI is performed along different diffusion-encoding directions, it is further observed in some organs that water diffusion exhibits directional dependence. This diffusion anisotropy occurs because for cells with very elongated geometries, water tends to diffuse more readily along the long axis of the cell than across the transverse axis. Also, ordered intracellular protein structures may contribute to diffusion anisotropy.

The existence of diffusion anisotropy means that the diffusion of water in organs such as muscle cannot be characterized using a scalar diffusion coefficient. Rather, a more complex mathematical model is required. DT-MRI, introduced by Basser *et al.* (41), is one such model. The diffusion tensor, **D**, is a 3×3, positive-definite, symmetric matrix with the diffusivities in the x, y, and z directions lying on the diagonal and their corresponding off-diagonal elements. DT-MRI requires diffusion-weighted MR signals to be acquired along at least six non-collinear directions. Along each diffusion-encoding direction, the signal varies according to:

$$S{=}S_0 \cdot e^{-b\mathbf{g}^{\mathrm{T}}\mathbf{D}\mathbf{g}} \quad (3)$$

where **g** is the direction of a diffusion-sensitizing gradient and the superscript T denotes matrix transposition. The tensor is formed using multiple regression, the options for which are described below.

Author Manuscript Author Manuscript Author Manuscript Author Manuscript

Diagonalization of **D** yields a 3×3 diagonal matrix of eigenvalues, which are the principal diffusivities of the fiber system. These eigenvalues are sorted on the basis of magnitude and are commonly symbolized λ_1, λ_2, and λ_3. The largest eigenvalue, λ_1, corresponds to water diffusion along the fiber axis; the intermediate and smallest eigenvalues (λ_2 and λ_3, respectively) correspond to water diffusion transverse to the fiber axis. The degree of difference among the eigenvalues reflects diffusion anisotropy, which can be characterized with the fractional anisotropy, FA:

$$\mathrm{FA}=\sqrt{\frac{3}{2}}\cdot\sqrt{\frac{(\lambda_1-\overline{\lambda})^2+(\lambda_2-\overline{\lambda})^2+(\lambda_3-\overline{\lambda})^2}{\lambda_1^2+\lambda_2^2+\lambda_3^2}} \quad (4)$$

where $\overline{\lambda}$ is the mean diffusivity, calculated as the average of λ_1, λ_2, and λ_3. Diagonalization of **D** also yields a matrix of three eigenvectors. The eigenvector matrix describes the rotation of the fiber system away from the imager's frame of reference. The three eigenvectors, symbolized $\mathbf{v}_1$, $\mathbf{v}_2$, and $\mathbf{v}_3$, indicate the directions associated with λ_1, λ_2, and λ_3, respectively.

Diffusion-Tensor MRI of Skeletal Muscle—Two important properties of water diffusion in skeletal muscle allow DT-MRI tracking to be performed. First, *D* for water in skeletal muscle fibers is lower than *D* in free water (42). Also, water diffuses approximately 40% more rapidly along skeletal muscle fiber's long axis than perpendicular to this axis (43). The reduction in *D* may result from the finite permeability of the cell membrane to water, an action of intracellular solid phase proteins as physical barriers to water displacement, and/or the transient binding of water to macromolecules and ions with smaller diffusion coefficients than that for free water (42, 44–46). Because sarcomeres are ~2–3 μm long but have an inter-filament spacing of ~30 nm, and because muscle fibers have a highly elongated overall geometry, there is a greater spatial frequency of diffusion-hindering structures in the transverse direction than in the longitudinal direction. This property contributes to diffusion anisotropy in muscle (44, 45). Indeed, recent work by Scheel *et al.* suggests that the higher FA and lower λ_2 and λ_3 values correspond to smaller fiber diameters (47). Studies in both skeletal (48, 49) and cardiac (50, 51) muscle have reported the correspondence of $\mathbf{v}_1$ to the histology-determined muscle fiber direction. It is this correspondence that allows DT-MRI fiber tracking to be used to represent skeletal muscle architecture.

DT-MRI DATA ACQUISITION: CONSIDERATIONS AND RECOMMENDATIONS

Sequence optimization

Hardware—Diffusion-weighted imaging of skeletal muscle does not require special hardware other than that used for standard imaging sequences. However, a few practical issues have to be considered. Multi-channel reception enables signal-to-noise ratio (SNR) efficient imaging with high parallel imaging acceleration factors, and multi-channel transmission can produce more homogeneous radiofrequency field distributions. For diffusion imaging of the brain, dedicated multi-channel head receiver coils, which can be

Author Manuscript Author Manuscript Author Manuscript Author Manuscript

conveniently placed in the iso-center of the magnet, are available. However, these coils are often not suitable for imaging skeletal muscle in the upper and lower extremities, and multi-coil arrays for imaging whole body segments may not be available. Consequently, sub-optimal coils may need to be used. Subject motion may cause non-uniform deformation in skeletal muscles and therefore it is crucial that the subject remains motionless during the experiment; strategies for reducing motion have been described in Refs. (52–54). In devising strategies to limit motion and when choosing coils, it is essential to ensure that the muscle of interest is not deformed. Moreover, it is often anatomically impossible to place the body part of interest in the iso-center of the magnet (55). Off-center placement at an angle to the main magnetic field will result in poor magnetic field homogeneity and associated image distortions. Accurate (image-based) shimming may improve image quality and partly reduce the need for unwarping images with post processing methods. Finally, imaging of complete muscles in arms or legs may require acquisitions in multiple stacks because the limb may be too long to fit in the homogeneous part of the MRI magnet (52, 56). Typically, each location within the body presents unique challenges with regard to subject positioning, shimming, radiofrequency coil type and placement, *etc.*

Sequence selection—Diffusion MRI methods have been applied extensively to image brain white matter fiber architecture and reveal microstructural changes or differences with neuropathology and treatment (57). From these studies, much theoretical and practical knowledge is available to optimize DT-MRI sequences with respect to b-value, diffusion-gradient directions, and general sequence parameters such as the repetition time (TR) and echo time (TE), to support the development of sufficient SNR for accurate parameter estimation and to limit artifacts (58). For DT-MRI applications outside the brain, for example skeletal muscle, this provides a solid theoretical basis for sequence optimization. Nevertheless, a number of practical issues and fundamental differences between brain and muscle must be considered in order to optimize sequence selection (59–61).

Single-shot echo-planar imaging (EPI) with Stejskal-Tanner diffusion-encoding is typically used for signal readout because EPI is fast, SNR-efficient, and relatively robust to motion. Also, this diffusion sequence implementation is readily available on most clinical scanners. However, a drawback of diffusion-weighted, single-shot EPI is that the TE can exceed 50 ms, as the time required for a single shot readout and the limited gradient strengths of clinical scanners collectively mean that high b-values only can be obtained at the expense of increasing the diffusion gradients' length and spacing. This usually is acceptable for brain diffusion imaging studies, but such TE values are long relative to the T_2 of muscle (~30 ms at 3T; (62)). At higher b-values, therefore, signal attenuation from T_2 decay leads to considerable signal loss. Low SNR results in overestimation of λ_1 and FA and underestimation of λ_3. Also, fiber tracking becomes inaccurate for SNR lower than 30 (59, 61). Therefore, an optimal b-value balances the effects of more accurate tensor estimation at higher b-values (which create larger differences in signal for the different diffusion directions) with decreased accuracy as a result of lower SNR (which occurs with increases in the TE). For the single-shot EPI readout with Stejskal-Tanner pulsed field gradients, a b-value between 400 and 500 s/mm^2 and a TE between 40 and 45 ms provide the most accurate diffusion parameter estimations and fiber tracking results (59, 61). Finally, the

Author Manuscript Author Manuscript Author Manuscript Author Manuscript

number of diffusion-encoding directions must be balanced with the number of signal averages: generally, using more diffusion-encoding directions is desirable, as long as the signals in the diffusion-weighted images exceed the noise floor (61, 63). It is recommended to acquire the number of diffusion-weighted and unweighted images with a ratio of approximately 8:1 (64).

The problem of a long TE being required to achieve high b-values can be solved by replacing the spin-echo preparation with a stimulated echo (STE) diffusion preparation (65). Because diffusion occurs during the mixing time (TM), higher b-values can be achieved with short TE values and low diffusion-encoding gradient strengths. Since the apparent muscle diffusion values and anisotropy depend on the diffusion time (66–68), increasing diffusion time by increasing TM will tend to increase FA and decrease the tensor eigenvalues. A longer TM, and thus higher FA, can provide higher accuracy in fiber tractography (69). Like other sequences, the STE sequence requires well optimized imaging parameters such as the TR, TM, TE, echo train length (for multi-shot approaches), and RF pulse characteristics (60, 65, 70). The STE preparation itself cannot provide more than 50% of the signal that can be obtained using SE preparations; however, a portion of this can be recovered using hyperechoes (71). Because T_1 relaxation occurs during the mixing time, a long TM value will reduce the SNR further (60, 65, 68). However, as we discuss below, this can be exploited to help mitigate the effects of fat signal contamination in EPI-based DT-MRI sequences.

Fat suppression—For several reasons, effective fat signal suppression is required in diffusion-tensor imaging. First, the presence of adipose tissue within the field of view leads to water-fat chemical shift artifact in the images. Because the phase of the signal continues to evolve during the long acquisition time used for single-shot image readout, chemical shift artifacts are particularly evident in the phase-encoding direction of EPI data. Also, a common pathological feature of many muscle diseases is progressive replacement of muscle by adipose tissue; increases in intramuscular fat also occur during healthy aging. Fat has a lower diffusivity than skeletal muscle and its diffusion is more isotropic (72); the presence of adipose tissue within muscle therefore complicates the interpretation of the diffusion parameters and may lead to errors in the specification of the direction of principal diffusion (59). Therefore, adequate fat suppression is essential for valid estimates of the diffusion tensor parameters of skeletal muscle. This is particularly important in the case of fat-infiltrating myopathies (73).

Fat suppression is commonly accomplished by selective saturation or inversion of the aliphatic and olefinic resonances by spectrally or spatial-spectrally selective pulses (74). Slice-selection gradient reversal methods (75) and water-selective excitation methods are also possible. Suppression of the olefinic protons by spectral saturation or inversion can be challenging because of their close proximity to the water peak. Alternative Dixon- (76, 77) or IDEAL- (78) type approaches have been proposed to remove olefinic fat without affecting the water resonance and to provide robustness to B_0 inhomogeneities. When STE sequences are used, the fact that the T_1/T_2 ratio is higher in muscle than in fat means that fat experiences greater T_1-mediated signal losses during the TM. This provides additional fat signal suppression. A robust approach, using a combination of methods, is typically

Author Manuscript Author Manuscript Author Manuscript Author Manuscript

required. When fat suppression is incomplete, the artifacts discussed above will persist and generally make that region unsuited for further analysis.

Even when the fat signal is effectively suppressed, some effects on the data can persist. These include a paradoxical elevation of the fractional anisotropy in voxels composed primarily of fat and an inaccurate and/or imprecise estimation of the direction of principal diffusion, as the suppression of fat signal effectively reduces the SNR (74). Also, fat replacement in myopathies is typically coincident with fibrosis. The effects of fibrosis on the estimation of the muscle diffusion tensor have not, to the authors' knowledge, been investigated.

DTI DATA ANALYSIS FOR MUSCLE STRUCTURAL CHARACTERIZATION

Initial processing steps

Registration/distortion correction—Fiber tracking requires that the tensor is estimated within each imaging voxel. For an accurate tensor estimation it is important therefore that each of the diffusion weighted volumes is spatially registered properly. Misregistration of the diffusion-weighted volumes may be caused by subject motion and eddy-current induced distortions. Strategies for limiting subject motion during data acquisition were considered in the previous section. Post-processing correction is done typically by using a 3D affine transformation, which is able to correct translation, rotation, scaling, and skewing of the diffusion-weighted volumes. Since affine registration affects the entire volume, only global affine distortions can be corrected with this approach.

Because diffusion-weighted imaging is typically performed using an EPI readout, the images will suffer from susceptibility induced distortions (79). The susceptibility-induced distortions will be similar for all diffusion-weighted volumes. However, the eddy current-induced distortions differ for each diffusion-weighted volume. As a result of these image deformations, the diffusion-weighted data may become misregistered with anatomical T_1- and T_2-weighted scans and suffer from local signal voids and signal pile-up. Several methods have been proposed to correct for susceptibility-induced distortions in EPI. A B_0 field can be recorded and used to correct the EPI readout for spatial deformations by creating a signal displacement map (55, 79). However the signal pileup cannot be corrected in this way. Alternatively, if an undistorted T_1- or T_2-weighted anatomical scan is available, correction can be performed using non-rigid registration of the diffusion data to the anatomical scan (80–82). Moreover, susceptibility distortions can be avoided using an EPI protocol with two acquisition of reversed phase encoding directions (83, 84), though we are not aware of this approach having been applied to skeletal muscle.

Smoothing/noise reduction methods—High SNR is important for accurate parameter estimation and fiber tracking (59, 61), but is difficult to realize because of the low T_2 of skeletal muscle. To decrease the destructive effect of noise on the tensor estimation and fiber tracking, various smoothing and noise-compensation algorithms have been proposed. Froeling *et al.* (55) used a Rician linear minimum mean square error (LMMSE) estimator (85) to suppress noise in the diffusion weighted images while preserving edges. Hiepe *et al.* used a multichannel Wiener filter with Rician bias correction (86). Buck *et al.* (87) applied

Author Manuscript Author Manuscript Author Manuscript Author Manuscript

an anisotropic smoothing algorithm (88) prior to fiber tracking and showed that this procedure results in fewer prematurely terminated fiber tracts and less local heterogeneity in the fiber orientation estimates. The effects of noise suppression and tensor regularization in skeletal muscle experiments have not been studied in great depth. However, there is substantial literature available on the comparison of various noise-suppression algorithms in brain diffusion imaging (89–91). Alternatively, noise regularization can be applied to the tensor field (92, 93). Levin *et al.* proposed a method to regularize the tensor field using the assumption that the skeletal muscle architecture is divergence free (94). A limitation of this method is that it can only be applied to regularize the fiber tracts and not the diffusion tensor eigenvalues and derived scalar indices.

Calculating the tensor—Before calculating the diffusion tensor, the b-matrix must be reoriented to account for subject motion (95). However, deformations due to eddy currents and B_0 inhomogenieties and concomitant fields require correction only for misregistration; the b-matrix need not be rotated (96). The diffusion tensor is commonly estimated by using multiple regression to regress the tensor elements on the observed signal intensities (97, 98).To date, the two most common methods used in skeletal muscle applications have been the Linear Least Squares (LLS) and the Weighted Linear Least Squares (WLLS) estimators (99). Here the logarithm of the diffusion weighted signal $S_{b,i}$ is defined as

$$\boldsymbol{y}=B\boldsymbol{\alpha}+\varepsilon \quad (5)$$

with

$$\begin{gathered}\boldsymbol{y_i}=\log(S_{b,i})\\ \boldsymbol{\alpha}=[\ln(S_0), D_{\mathrm{xx}}, D_{\mathrm{yy}}, D_{\mathrm{zz}}, D_{\mathrm{xy}}, D_{\mathrm{yz}}]\\ \boldsymbol{B_i}=\left(1, -b_i g_{x,i}^2, -b_i g_{y,i}^2, -b_i g_{z,i}^2, -2b_i g_{x,i} g_{y,i}, -2b_i g_{x,i} g_{z,i}, -2b_i g_{y,i} g_{z,i}\right)\end{gathered}$$

where ε_i is the independent error term. The LLS estimator of $\boldsymbol{\gamma}$ is defined as $\hat{\boldsymbol{\alpha}}=(B^TB)^{-1}B^Ty$, whereas the WLLS estimator is $\hat{\boldsymbol{\alpha}}=(B^TWB)^{-1}B^TWy$, with $W=\mathrm{diag}(S_{b,i}^2)$. The advantages of using the LLS and WLLS methods is that they are computationally efficient and easy to implement. In addition to the LLS and WLLS methods, it is also possible to use a Non-Linear Squares estimator, which is solved typically using a Levenberg-Marquardt approach. The diffusion tensor is assumed to contain real positive eigenvalues (e.g. symmetric positive definite). However due to noise or artifact, non-positive definite tensors may be found. Several other methods have been proposed for robust tensor estimation in the presence of noise, e.g. constrained LLS, WLLS and NLS (97), RESTORE (100), and REKINDLE (101). However, these estimators are not commonly used for skeletal muscle applications.

Quality control of initially processed data—This discussion has highlighted several important issues related to the quality of DT-MRI data from skeletal muscle and some initial processing steps that can be taken to mitigate these problems. A comprehensive list of potential problems related to data acquisition and processing is listed here (58). The authors

Author Manuscript Author Manuscript Author Manuscript Author Manuscript

recommend that before proceeding with the fiber tracking procedures to be described in the next section, the raw data and initially processed data be quantitatively assessed with these issues in mind. The next section also describes quality control measures for fiber tracking outcomes.

Fiber tracking

Fiber tracking: seeding, propagation and selection—Skeletal muscle fiber tracking maps the fiber trajectories between the origin and insertion of the muscle. Two broad classes of fiber tracking algorithms have been described: probabilistic and deterministic. Probabilistic algorithms use Monte Carlo methods to predict the most likely paths of connectivity between two structures (e.g., (102–106)). The salient feature of probabilistic methods is that, at each tracking step, the fiber direction is not deterministically computed, but rather is randomly sampled from the distribution function of the principal eigenvector. Fiber tracking in this manner allows uncertainties from partial volume averaging and image noise to be considered. Implementation of probabilistic fiber tracking involves many repeated trials, typically in the range of 1000 to 5000, for each seed point, yielding a map of connection probability density for the seed point.

The other class of tracking algorithms involves deterministic methods, and it is these approaches that have been applied to skeletal muscle. In this approach fiber tracking is commonly initiated from a set of seed points, which can be defined based on a region, surface, or volume of interest. Each point in the set is described with $\{x, y, z\}$ coordinates and is the starting point for a fiber tract. A muscle-specific approach to seed point definition, described by Lansdown *et al.* (52), is to define the aponeurosis of insertion as the seed surface and propagate the tracts from this surface. As described in the section below, this approach facilitates some aspects of structural characterization. Seed points may be defined at even spacing, *e.g.* seeding of one point every mm^3 or voxel, or this spacing may be defined *post hoc* (107). From every seed point, tracts propagate with a predefined step size, which is usually smaller than the voxel dimension. The fiber tracts may be propagated bidirectionally if the seeding surface is located within the muscle, while the fiber tracts will propagate unidirectionally if the seeding surface represents the origin or insertion of the muscle fibers (as in Ref. (52). There are several approaches to determining the direction of propagation (see Ref. (108) for a review). Except for two preliminary studies (109, 110), the impact of the deterministic tracking algorithm on fiber tracking outcomes has not been extensively examined for muscle applications.

Tract propagation continues until pre-defined stopping criteria are met. These criteria may be based on anatomical boundaries (for example, terminating the tracts at the muscle borders). Or, they may be based on properties of the data that imply low confidence in the diffusion direction estimates such as minimal/maximal FA values and maximum angle change per propagation step (that is, a seeded and initially propagated fiber tract will be terminated if the FA or angle change per step falls outside of a pre-determined range). Although these are the most commonly used criteria, the stopping criteria can be any geometrical value or scalar obtained from the DT-MRI measurement or a separate anatomical MRI scan.

Author Manuscript Author Manuscript Author Manuscript Author Manuscript

Impact of tracking criteria on outcomes—Stopping criteria and seed point selection can have significant effects on the fiber tracking outcomes. Choosing the right stopping criteria can be challenging, since different muscles can have different FA (111) and curvature values. Furthermore, the water diffusion properties may change in pathology (72). Thus, the stopping criteria may need to be adjusted so that the tracking results reflect the underlying architecture accurately. Figure 3 shows the effect of changing the FA and angle per propagation step on tracking results of the tibialis anterior muscle. Reducing the allowable propagation angle criterion from ≤300 (Fig. 3B and 3D) to ≤100 (Fig. 3A and 3C) per 1.5 mm tracking step will reduce spurious fiber tracts, as shown in the white circles. However, making this stop criterion too strict could stop fiber tracking in highly curved musles prematurely. Changing the trackable FA range from a conservative range of 0.20–0.50 (Fig. 3A and 3B) to 0.15–0.75 (Fig. 3C and 3D) will allow for more and longer fiber tracts, as indicated in the white rectangle. However, the trade-off for this overall increase in the number of tracts may be a corresponding increase in the number of erroneous tracts (as indicated by the tracts that seem to continue through the bone; see Fig. 3D).

The manner in which fiber tracts are seeded also influences the fiber tracking outcome (Fig. 4). Most fiber tracking software allow the use of seed regions as well as whole volume (WV) seeding followed by fiber tract selection using the Boolean operators AND, NOT, and OR. Tract selection based on WV fiber tracking typically results in a more homogeneous and dense tract distribution. In Fig 4A and 4C, the tracts were seeded by the yellow planar region. Alternatively, in Fig. 4B and 4C, WV seeding was used. In Fig. 4B, only those tracts passing through the yellow region are visualized. Selection of fiber tracts is not limited to a single region. In Fig. 4C, the tracts originate from the yellow region, after which only those that pass through both green regions are selected. Selections of the WV tracts using the same two green regions are shown in Fig. 4D. In general, the right combination of Boolean selection regions allows one to refine fiber tracking results in cases where the chosen stopping criteria are not sufficient to prevent spurious tracts. We emphasize that when using criteria such as these, they should be based on accepted patterns of muscle structure and function, and they should be applied systematically.

Finally, it is important to apply quality control standards to the fiber tracking outcomes, as problems such as prematurely terminating tracts, fibers that exit the muscle borders, and artifacts or low SNR leading to erroneous specification of the principal direction of diffusion may occur. One such approach, proposed by Heemskerk *et al.* (112), is based on criteria of minimum fiber tract length, whether or not the fibers extend near to (but not through) the boundary of the muscle or muscle compartment, and the agreement of the fiber tracking outcome with predictable architectural features of muscle such as the absence of abrupt changes in curvature within a tract and of local similarity in all observed structural properties. These authors found that when applying these criteria, between 75 and 90% of the initially propagated fiber tracts were preserved.

Structural characterization

Some of the muscle architectural data of interest in biomechanics studies include fiber or fascicle length, θ, and κ. Each of these parameters can be estimated using fiber tracking

Author Manuscript Author Manuscript Author Manuscript Author Manuscript

data. Although fiber tract visualization will depict a DT-MRI fiber tract as a continuous line, the tracts are in fact set **P** of *N* discrete points:

$$\mathbf{P}=\{p_1, p_2, p_3 \ldots p_N\}, \quad (6)$$

where p_n describes the nth point's {*x, y, z*} coordinates with a unit of distance from the origin of the laboratory frame of reference. These data can be used to estimate fascicle length, θ, and κ using the procedures described below.

Fiber tract smoothing—Damon *et al.* (113) demonstrated that for even high SNR levels, accurately estimating κ requires that the originally propagated fiber tracts must be smoothed, and they demonstrated the efficacy of polynomial fitting for this purpose. This procedure was shown not to affect the measurements of either fiber tract length (L_{ft}) or θ. Therefore, this procedure is recommended prior to performing any muscle architectural characterization. To do so, the *x, y*, and *z* coordinates of all points in **P** are separately fitted as functions of point number to 2nd order polynomial functions. Muscle fascicles may have more than a single direction of curvature (114), so a higher polynomial order may be required in some instances. However, the polynomial order should be kept to the minimum necessary to avoid introducing additional points of inflection in the fitted tracts erroneously.

Fiber length—The fiber tract length is analogous to the fascicle length measurements made using US imaging. To calculate L_{ft}, a position vector is formed between each successive pair of fitted points. Then, L_{ft} is determined as the sum of the position vector lengths along the length of the fiber tract. Bolsterlee *et al.* compared the L_{ft} measurements obtained from DT-MRI with fascicle length measurements from US and found that they agreed to within a mean difference of 3 mm, indicating good agreement; but they also observed a relatively poor precision of 10 mm (~20% of the mean fascicle length) (115). Heemskerk *et al.* analyzed the reproducibility of L_{ft} measurements and found them to be sufficiently reproducible for measuring practically significant alterations in muscle architecture (116).

Pennation angle—In 2-D US imaging studies, θ is estimated as the angle formed by a line tangent to the aponeurosis of muscle fiber insertion and a line tangent to the fascicle, at the point of insertion (Fig. 2). Lansdown *et al.* extended these methods to the 3-D space in MRI (52). As noted above, the fiber tracking method described by these authors uses a mesh reconstruction of the aponeurosis to define seed points for fiber tracking. This procedure has facilitated the use of DT-MRI fiber tracking data for pennation angle determinations. The procedure is illustrated in Fig. 5 and described below.

First, the orientation of the aponeurosis at the seed point is described by calculating the tangent plane to that point and the unit normal vector to this plane, n̂. A tangent plane is defined by two tangent lines that intersect at the seed point. Several approaches have been used to determine the tangent lines (52, 113). Regardless of how the equations of the tangent lines are estimated, the next step is to use the equations of the tangent lines to determine the equation of the tangent plane and n̂. Next, position vectors $\mathbf{r}_n$ are defined between the seed

Author Manuscript Author Manuscript Author Manuscript Author Manuscript

point and points along the fiber tract; these are converted to unit vectors (denoted $\hat{r}_n$). For each point *n* on the fiber tract, θ is determined as the complement to the angle formed by $\hat{n}$ and $\hat{r}_n$. The final value of θ is determined as the average of the values for θ from the first five fiber tract points (112). Damon *et al.* demonstrated the agreement of DT-MRI-based θ measurements with those values obtained by direct anatomical inspection (117), and these procedures were also verified using simulated data sets (113). Bolsterlee *et al.* observed a relative underestimation of US-measured values of θ compared to DT-MRI, but only directly under the US probe head; this suggested that tissue deformation associated with the US acquisition may have been the source of disagreement (115). Heemskerk *et al.* found that DT-MRI-based θ measurements are sufficiently reproducible for measuring practically significant alterations in muscle architecture (116).

Curvature—Several methods have been used to calculate κ from DT-MRI fiber tracking data. Froeling *et al.* used a three-point approximation of κ (61). In this approach, κ is estimated as the reciprocal of the radius of the circle that passes through the points $\{p_{(n-1)}\, p_n\, p_{(n+1)}\}$. Froeling *et al.* found that even for high SNR levels, κ tended to be overestimated; this was particularly true when κ was calculated over a small number of points. Damon *et al.* used a discrete implementation of the Frenet formulas (118). First, the unit tangent vector ($\hat{T}_{pn}$) between a pair of consecutive points p'_n and $p'_{(n-1)}$ is calculated. The tangent vector for the subsequent pair of points, $\hat{T}_{n+1}$, also was calculated. The spatial rate of change in the two unit tangent vectors, $\frac{\Delta \hat{\mathbf{T}}}{\Delta p}$, is used to calculate the unit normal vector $\hat{N}$ at the point *n*. Curvature can then be calculated as $\hat{\mathbf{N}}^{+}\frac{\Delta \mathbf{T}}{\Delta p}=\kappa$, where $\hat{\mathbf{N}}^{+}$ is the Moore-Penrose pseudoinverse matrix of $\hat{N}$. These calculations are repeated in a pointwise basis along the fiber tract. These procedures, when performed on the polynomial-fitted tracts, allowed κ to be estimated accurately for all values of κ up to and including 11.8 m^{-1}, for SNR levels as low as 50.

DT-MRI AND DT-MRI FIBER TRACKING APPLICATIONS

Muscle fiber tracking has been used to assess the structure of a variety of small animal muscles and human muscles. *In vivo* small animal studies in the rat gastrocnemius provided validation of the pennation angle measurements (117); in the mouse hindlimb, Heemskerk *et al.* calculated the PCSA (119). Applications of DT-MRI-based fiber tracking to human muscles include the plantarflexor (53, 92, 93, 120) and tibialis anterior (52, 112, 116) muscles of the leg, the quadriceps muscles of the thigh (68, 107, 121, 122), the forearm muscles (94), and the muscles of the female pelvic floor (123). Clinically relevant applications of fiber tracking include examining structural changes in the genioglossus muscle due to oral appliance use (124), studying the effects of chronic lateral patella dislocation (107), and examining age-associated changes in muscle architecture (125).

DT-MRI fiber tracking can provide new insights into muscle structure. For example, in the tibialis anterior muscle, Lansdown *et al.* observed larger values of θ in the superior portion of the muscle than in the inferior portion (52). Although a 3-D US study demonstrated such heterogeneity (27), this finding had not been reported previously in the 2-D US literature

Author Manuscript Author Manuscript Author Manuscript Author Manuscript

(33, 126). This heterogeneity was related to changes in the aponeurosis's orientation within the axial plane (52). Heterogeneity in L_{ft} has also been reported using DT-MTI tracking methods (116, 127), and preliminary reports indicate that θ and curvature decrease and L_{ft} increases upon muscle elongation (127, 128). Schwenzer *et al.* (129) and Sinha *et al.* (93) reported changes in the orientation of $\mathbf{v}_1$ due to muscle lengthening (which, by extension, correspond to changes in θ). These data indicate that DT-MRI and DT-MRI-based fiber tracking can provide new insights into muscle architecture not obtainable via 2-D imaging methods that do not use a fixed frame of reference. Also, when proper positioning procedures are used, DT-MRI is not subject to experimental errors such as the muscle deformation caused by US probe placement (115).

There are a few studies in which DT-MRI fiber tractography, in conjunction with other methods, was used to predict and investigate the active mechanics of muscle. Muscle deformation during contraction can be characterized by a strain tensor. Felton *et al.* used DT-MRI to assess the tongue's architecture and combined this with phase contrast MRI to measure strain rates in the tongue during swallowing. This enabled them to relate the architecture of the intrinsic and extrinsic muscles of the tongue with the manner in which the tongue deformed during swallowing (130). Englund *et al.* used spatial tagging MRI to estimate the 3-D strain tensor associated with isometric contraction of the tibialis anterior (131). Diagonalizing the strain tensor resulted in one negative strain and one positive strain (denoted ε_N and ε_P, respectively). The azimuthal direction corresponding to ε_N was associated with the muscle fiber direction, but had a lower angle of elevation over the XY plane than the fibers. Finally, Levin *et al.* used DT-MRI data to generate musculoskeletal models (132). These initial efforts illustrate the potential for combining functional MRI or other computational methods and DT-MRI-based muscle architectural information to obtain new insights into muscle structure-function relationships. One issue that should be incorporated into future studies is the development of methods to determine the architecture of the muscle during the active state, for example by combining DT-MRI fiber tracking with spatial tagging or velocity-encoded phase-contrast MRI methods.

CONCLUSIONS AND FUTURE RESEARCH AND DEVELOPMENT NEEDS

This review presents the rationale, structural basis, data acquisition methods, and data analysis methods for DT-MRI fiber tracking studies of skeletal muscle. This approach can provide new insights into muscle structure not available through other methods. In conjunction with the wide range of other measurement capabilities available through other physiological MRI methods, DT-MRI can be used to understand how the structural and functional properties of skeletal muscle are related. To close, we present several future research directions that are needed to realize fully the potential for DT-MRI skeletal muscle fiber tracking:

- Widespread dissemination of muscle-specific DT-MRI software tools;
- Determination and validation of the best approaches for acquiring, generating, and analyzing DT-MRI fiber tracking data under conditions of fat infiltration;

Author Manuscript Author Manuscript Author Manuscript Author Manuscript

- A systematic validation of DT-MRI-derived muscle architecture measurements across a wide range of muscle structural and data acquisition and analysis conditions, such as has been performed in the brain (e.g., Ref. (133–136));
- Determination and validation of the best approaches for using DT-MRI fiber tracking to quantify muscle architecture in the active state; and
- Development of approaches for synthesizing DT-MRI fiber tracking and other types of functional imaging data.

The existing strengths of DT-MRI fiber tracking, coupled with continued advancements of this kind, will favor the continued use of DT-MRI to generate new knowledge concerning the relationships among muscle structure and function, in health and disease.

Grant acknowledgements

NIH/NIAMS R01 AR050101, NIH/NIAMS R01 AR05709, Grant 1203-055 from the Nuts-Ohra Foundation (Amsterdam, The Netherlands), and the European Union COST Action BM1304

ABBREVIATIONS

CSA	cross-sectional area
B-mode	brightness mode
DT-MRI	diffusion tensor MRI
DW-MRI	diffusion weighted MRI
ECM	extracellular matrix
EPI	echo planar imaging
FA	fractional anisotropy
LLS	linear least squares
LMMSE	linear minimum mean squares error
PCSA	physiological cross-sectional area
SNR	signal-to-noise ratio
SR	sarcoplasmic reticulum
STE	stimulated echo
TM	mixing time
US	ultrasound
WLLS	weighted linear least squares
WV	whole volume

Author Manuscript Author Manuscript Author Manuscript Author Manuscript

REFERENCES

1. Aquin L, Lechner AJ, Sillau AH, Banchero N. Analysis of the shape changes of muscle fiber cross sections in guinea pigs raised at 22 degrees C and 5 degrees C. Pflugers Arch. 1980; 385(3):223–228. [PubMed: 7190684]
2. Polgar J, Johnson MA, Weightman D, Appleton D. Data on fibre size in thirty-six human muscles: An autopsy study. J Neurol Sci. 1973; 19(3):307–318. [PubMed: 4716847]
3. Ward SR, Eng CM, Smallwood LH, Lieber RL. Are current measurements of lower extremity muscle architecture accurate? Clin Orthop Relat Res. 2009; 467(4):1074–1082. [PubMed: 18972175]
4. Landis CS, Li X, Telang FW, Molina PE, Palyka I, Vetek G, Springer CS Jr. Equilibrium transcytolemmal water-exchange kinetics in skeletal muscle in vivo. Magn Reson Med. 1999; 42(3): 467–478. [PubMed: 10467291]
5. Trotter JA, Purslow PP. Functional morphology of the endomysium in series fibered muscles. J Morphol. 1992; 212(2):109–122. [PubMed: 1608046]
6. Lieber RL, Friden J. Functional and clinical significance of skeletal muscle architecture. Muscle Nerve. 2000; 23(11):1647–1666. [PubMed: 11054744]
7. Lieber RL, Friden J. Clinical significance of skeletal muscle architecture. Clin Orthop Relat Res. 2001; 383:140–151.
8. Winters TM, Takahashi M, Lieber RL, Ward SR. Whole muscle length-tension relationships are accurately modeled as scaled sarcomeres in rabbit hindlimb muscles. Journal of Biomechanics. 44(1):109–115.
9. Bodine SC, Roy RR, Meadows DA, Zernicke RF, Sacks RD, Fournier M, Edgerton VR. Architectural, histochemical, and contractile characteristics of a unique biarticular muscle: the cat semitendinosus. J Neurophysiol. 1982; 48(1):192–201. [PubMed: 7119845]
10. Powell PL, Roy RR, Kanim P, Bello MA, Edgerton VR. Predictability of skeletal muscle tension from architectural determinations in guinea pig hindlimbs. J Appl Physiol. 1984; 57(6):1715–1721. [PubMed: 6511546]
11. Hill AV. The pressure developed in muscle during contraction. The Journal of Physiology. 1948; 107(4):518–526. [PubMed: 16991832]
12. Sejersted OM, Hargens AR, Kardel KR, Blom P, Jensen O, Hermansen L. Intramuscular fluid pressure during isometric contraction of human skeletal muscle. J Appl Physiol. 1984; 56(2):287–295. [PubMed: 6706739]
13. Otten E. Concepts and models of functional architecture in skeletal muscle. Exerc Sport Sci Rev. 1988; 16:89–137. [PubMed: 3292268]
14. Van Leeuwen JL, Spoor CW. Modelling mechanically stable muscle architectures. Philos Trans R Soc Lond B Biol Sci. 1992; 336(1277):275–292. [PubMed: 1353268]
15. Van Leeuwen JL, Spoor CW. Modelling the pressure and force equilibrium in unipennate muscles with in-line tendons. Philos Trans R Soc Lond B Biol Sci. 1993; 342(1302):321–333. [PubMed: 8115452]
16. Miura H, McCully K, Nioka S, Chance B. Relationship between muscle architectural features and oxygenation status determined by near infrared device. Eur J Appl Physiol. 2004; 91(2–3):273–278. [PubMed: 14574577]
17. Pappas GP, Asakawa DS, Delp SL, Zajac FE, Drace JE. Nonuniform shortening in the biceps brachii during elbow flexion. J Appl Physiol. 2002; 92(6):2381–2389. [PubMed: 12015351]
18. Finni T, Hodgson JA, Lai AM, Edgerton VR, Sinha S. Nonuniform strain of human soleus aponeurosis-tendon complex during submaximal voluntary contractions in vivo. J Appl Physiol. 2003; 95(2):829–837. [PubMed: 12716873]
19. Finni T, Hodgson JA, Lai AM, Edgerton VR, Sinha S. Mapping of movement in the isometrically contracting human soleus muscle reveals details of its structural and functional complexity. J Appl Physiol. 2003; 95(5):2128–2133. [PubMed: 12857769]
20. Lee HD, Finni T, Hodgson JA, Lai AM, Edgerton VR, Sinha S. Soleus aponeurosis strain distribution following chronic unloading in humans: an in vivo MR phase-contrast study. J Appl Physiol. 2006; 100(6):2004–2011. [PubMed: 16424072]

Author Manuscript Author Manuscript Author Manuscript Author Manuscript

21. Shin DD, Hodgson JA, Edgerton VR, Sinha S. In vivo intramuscular fascicle-aponeuroses dynamics of the human medial gastrocnemius during plantarflexion and dorsiflexion of the foot. J Appl Physiol. 2009; 107(4):1276–1284. [PubMed: 19608924]
22. Blemker SS, Pinsky PM, Delp SL. A 3D model of muscle reveals the causes of nonuniform strains in the biceps brachii. J Biomech. 2005; 38(4):657–665. [PubMed: 15713285]
23. Chi S-W, Hodgson J, Chen J-S, Reggie Edgerton V, Shin DD, Roiz RA, Sinha S. Finite element modeling reveals complex strain mechanics in the aponeuroses of contracting skeletal muscle. Journal of Biomechanics. 43(7):1243–1250.
24. Wickiewicz TL, Roy RR, Powell PL, Edgerton VR. Muscle architecture of the human lower limb. Clin Orthop Relat Res. 1983; 179:275–283.
25. Gordon AM, Huxley AF, Julian FJ. The variation in isometric tension with sarcomere length in vertebrate muscle fibres. J Physiol. 1966; 184(1):170–192. [PubMed: 5921536]
26. Rutherford OM, Jones DA. Measurement of fibre pennation using ultrasound in the human quadriceps in vivo. Eur J Appl Physiol Occup Physiol. 1992; 65(5):433–437. [PubMed: 1425649]
27. Hiblar, T., Bolson, EL., Hubka, M., Sheehan, FH., Kushmerick, MJ. Molecular Aspects Cellular Contraction of Muscle. Three dimensional ultrasound analysis of fascicle orientation in human tibialis anterior muscle enables analysis of macroscopic torque at the cellular level. In: Sugi, H., editor. Volume 538, Advances in Experimental Medicine and Biology. New York, NY: Springer; 2003. p. 635-645.
28. Weinstein MM, Jung S-A, Pretorius DH, Nager CW, den Boer DJ, Mittal RK. The reliability of puborectalis muscle measurements with 3-dimensional ultrasound imaging. American Journal of Obstetrics and Gynecology. 2007; 197(1):68.e61–68.e66. [PubMed: 17618762]
29. Kurihara T, Oda T, Chino K, Kanehisa H, Fukunaga T. Use of three-dimensional ultrasonography for the analysis of the fascicle length of human gastrocnemius muscle during contractions. International Journal of Sport and Health Science. 2005; 3:226–234.
30. Fukunaga T, Ichinose Y, Ito M, Kawakami Y, Fukashiro S. Determination of fascicle length and pennation in a contracting human muscle in vivo. J Appl Physiol. 1997; 82(1):354–358. [PubMed: 9029238]
31. Ito M, Kawakami Y, Ichinose Y, Fukashiro S, Fukunaga T. Nonisometric behavior of fascicles during isometric contractions of a human muscle. J Appl Physiol. 1998; 85(4):1230–1235. [PubMed: 9760310]
32. Muramatsu T, Muraoka T, Kawakami Y, Shibayama A, Fukunaga T. In vivo determination of fascicle curvature in contracting human skeletal muscles. J Appl Physiol. 2002; 92(1):129–134. [PubMed: 11744651]
33. Maganaris CN, Baltzopoulos V. Predictability of in vivo changes in pennation angle of human tibialis anterior muscle from rest to maximum isometric dorsiflexion. Eur J Appl Physiol Occup Physiol. 1999; 79(3):294–297. [PubMed: 10048637]
34. Maganaris CN, Paul JP. Load-elongation characteristics of in vivo human tendon and aponeurosis. J Exp Biol. 2000; 203(Pt 4):751–756. [PubMed: 10648216]
35. Lopata RGP, van Dijk JP, Pillen S, Nillesen MM, Maas H, Thijssen JM, Stegeman DF, de Korte CL. Dynamic imaging of skeletal muscle contraction in three orthogonal directions. Journal of Applied Physiology. 109(3):906–915.
36. Cronin NJ, Lichtwark G. The use of ultrasound to study muscle-tendon function in human posture and locomotion. Gait & posture. 2013; 37(3):305–312. [PubMed: 22910172]
37. Le Bihan D, Mangin JF, Poupon C, Clark CA, Pappata S, Molko N, Chabriat H. Diffusion tensor imaging: concepts and applications. J Magn Reson Imaging. 2001; 13(4):534–546. [PubMed: 11276097]
38. Le Bihan D. Molecular diffusion nuclear magnetic resonance imaging. Magn Reson Q. 1991; 7(1): 1–30. [PubMed: 2043461]
39. Lazar M, Weinstein DM, Tsuruda JS, Hasan KM, Arfanakis K, Meyerand ME, Badie B, Rowley HA, Haughton V, Field A, Alexander AL. White matter tractography using diffusion tensor deflection. Hum Brain Mapp. 2003; 18(4):306–321. [PubMed: 12632468]
40. Stejskal E, Tanner J. Spin diffusion measurements: spin echoes in the presence of a time-dependent field gradient. J Chem Phys. 1965; 42:288–292.

Author Manuscript Author Manuscript Author Manuscript Author Manuscript

41. Basser PJ, Mattiello J, LeBihan D. MR diffusion tensor spectroscopy and imaging. Biophys J. 1994; 66(1):259–267. [PubMed: 8130344]
42. Finch ED, Harmon JF, Muller BH. Pulsed NMR measurements of the diffusion constant of water in muscle. Arch Biochem Biophys. 1971; 147(1):299–310. [PubMed: 5114937]
43. Cleveland GG, Chang DC, Hazlewood CF, Rorschach HE. Nuclear magnetic resonance measurement of skeletal muscle: anisotropy of the diffusion coefficient of the intracellular water. Biophys J. 1976; 16(9):1043–1053. [PubMed: 963204]
44. Rorschach HE, Chang DC, Hazlewood CF, Nichols BL. The diffusion of water in striated muscle. Ann N Y Acad Sci. 1973; 204:445–452. [PubMed: 4350249]
45. Chang DC, Rorschach HE, Nichols BL, Hazlewood CF. Implications of diffusion coefficient measurements for the structure of cellular water. Ann N Y Acad Sci. 1973; 204:434–443. [PubMed: 4350248]
46. Clark ME, Burnell EE, Chapman NR, Hinke JA. Water in barnacle muscle IV. Factors contributing to reduced self-diffusion. Biophys J. 1982; 39(3):289–299. [PubMed: 7139028]
47. Scheel M, von Roth P, Winkler T, Arampatzis A, Prokscha T, Hamm B, Diederichs G. Fiber type characterization in skeletal muscle by diffusion tensor imaging. NMR in Biomedicine. 2013; 26(10):1220–1224. [PubMed: 23553895]
48. Van Donkelaar CC, Kretzers LJ, Bovendeerd PH, Lataster LM, Nicolay K, Janssen JD, Drost MR. Diffusion tensor imaging in biomechanical studies of skeletal muscle function. J Anat. 1999; 194(Pt 1):79–88. [PubMed: 10227669]
49. Napadow VJ, Chen Q, Mai V, So PT, Gilbert RJ. Quantitative analysis of three-dimensional-resolved fiber architecture in heterogeneous skeletal muscle tissue using nmr and optical imaging methods. Biophys J. 2001; 80(6):2968–2975. [PubMed: 11371469]
50. Hsu EW, Muzikant AL, Matulevicius SA, Penland RC, Henriquez CS. Magnetic resonance myocardial fiber-orientation mapping with direct histological correlation. Am J Physiol. 1998; 274(5 Pt 2):H1627–H1634. [PubMed: 9612373]
51. Scollan DF, Holmes A, Winslow R, Forder J. Histological validation of myocardial microstructure obtained from diffusion tensor magnetic resonance imaging. Am J Physiol. 1998; 275(6 Pt 2):H2308–H2318. [PubMed: 9843833]
52. Lansdown DA, Ding Z, Wadington M, Hornberger JL, Damon BM. Quantitative diffusion tensor MRI-based fiber tracking of human skeletal muscle. J Appl Physiol. 2007; 103(2):673–681. [PubMed: 17446411]
53. Sinha S, Sinha U, Edgerton VR. In vivo diffusion tensor imaging of the human calf muscle. J Magn Reson Imaging. 2006; 24(1):182–190. [PubMed: 16729262]
54. Froeling M, Oudeman J, van den Berg S, Nicolay K, Maas M, Strijkers GJ, Drost MR, Nederveen AJ. Reproducibility of diffusion tensor imaging in human forearm muscles at 3.0 T in a clinical setting. Magn Reson Med. 2010; 64(4):1182–1190. [PubMed: 20725932]
55. Froeling M, Nederveen AJ, Heijtel DF, Lataster A, Bos C, Nicolay K, Maas M, Drost MR, Strijkers GJ. Diffusion-tensor MRI reveals the complex muscle architecture of the human forearm. J Magn Reson Imaging. 2012; 36(1):237–248. [PubMed: 22334539]
56. Froeling M, Oudeman J, Strijkers GJ, Maas M, Drost MR, Nicolay K, Nederveen AJ. Muscle changes detected with diffusion-tensor imaging after long-distance running. Radiology. 2015; 274(2):548–562. [PubMed: 25279435]
57. Abhinav K, Yeh FC, Pathak S, Suski V, Lacomis D, Friedlander RM, Fernandez-Miranda JC. Advanced diffusion MRI fiber tracking in neurosurgical and neurodegenerative disorders and neuroanatomical studies: A review. Biochim Biophys Acta. 2014; 1842(11):2286–2297. [PubMed: 25127851]
58. Jones DK, Cercignani M. Twenty-five pitfalls in the analysis of diffusion MRI data. NMR Biomed. 2010; 23(7):803–820. [PubMed: 20886566]
59. Damon BM. Effects of image noise in muscle diffusion tensor (DT)-MRI assessed using numerical simulations. Magn Reson Med. 2008; 60(4):934–944. [PubMed: 18816814]
60. Karampinos DC, Banerjee S, King KF, Link TM, Majumdar S. Considerations in high-resolution skeletal muscle diffusion tensor imaging using single-shot echo planar imaging with stimulated-

Author Manuscript Author Manuscript Author Manuscript Author Manuscript

echo preparation and sensitivity encoding. NMR Biomed. 2012; 25(5):766–778. [PubMed: 22081519]

61. Froeling M, Nederveen AJ, Nicolay K, Strijkers GJ. DTI of human skeletal muscle: the effects of diffusion encoding parameters, signal-to-noise ratio and T2 on tensor indices and fiber tracts. NMR in Biomedicine. 2013; 26(11):1339–1352. [PubMed: 23670990]
62. Gold GE, Han E, Stainsby J, Wright G, Brittain J, Beaulieu C. Musculoskeletal MRI at 3.0 T: relaxation times and image contrast. AJR Am J Roentgenol. 2004; 183(2):343–351. [PubMed: 15269023]
63. Rockel C, Noseworthy MD. An exploration of diffusion tensor eigenvector variability within human calf muscles. Journal of Magnetic Resonance Imaging 2015:n/a-n/a.
64. Jones DK, Horsfield MA, Simmons A. Optimal strategies for measuring diffusion in anisotropic systems by magnetic resonance imaging. Magn Reson Med. 1999; 42(3):515–525. [PubMed: 10467296]
65. Steidle G, Schick F. Echoplanar diffusion tensor imaging of the lower leg musculature using eddy current nulled stimulated echo preparation. Magn Reson Med. 2006; 55(3):541–548. [PubMed: 16450364]
66. Kim S, Chi-Fishman G, Barnett AS, Pierpaoli C. Dependence on diffusion time of apparent diffusion tensor of ex vivo calf tongue and heart. Magn Reson Med. 2005; 54(6):1387–1396. [PubMed: 16265644]
67. Sigmund EE, Novikov DS, Sui D, Ukpebor O, Baete S, Babb JS, Liu K, Feiweier T, Kwon J, McGorty K, Bencardino J, Fieremans E. Time-dependent diffusion in skeletal muscle with the random permeable barrier model (RPBM): application to normal controls and chronic exertional compartment syndrome patients. NMR Biomed. 2014; 27(5):519–528. [PubMed: 24610770]
68. Noehren B, Andersen A, Feiweier T, Damon B, Hardy P. Comparison of twice refocused spin echo versus stimulated echo diffusion tensor imaging for tracking muscle fibers. Journal of Magnetic Resonance Imaging. 2015; 41(3):624–632. [PubMed: 24554376]
69. Sigmund EE, Sui D, Ukpebor O, Baete S, Fieremans E, Babb JS, Mechlin M, Liu K, Kwon J, McGorty K, Hodnett PA, Bencardino J. Stimulated echo diffusion tensor imaging and SPAIR T2 - weighted imaging in chronic exertional compartment syndrome of the lower leg muscles. J Magn Reson Imaging. 2013; 38(5):1073–1082. [PubMed: 23440764]
70. Schick F. Signal losses in diffusion preparation: comparison between spin-echo, stimulated echo and SEASON. MAGMA. 1998; 6(1):53–61. [PubMed: 9794290]
71. Frank L, Wong E, Liu T, Buxton R. Increased Diffusion Sensitivity With Hyperechos. Magn Reson Med. 2003; 49:1098–1105. [PubMed: 12768588]
72. Qi J, Olsen NJ, Price RR, Winston JA, Park JH. Diffusion-weighted imaging of inflammatory myopathies: polymyositis and dermatomyositis. J Magn Reson Imaging. 2008; 27(1):212–217. [PubMed: 18022843]
73. Hooijmans MT, Damon BM, Froeling M, Versluis MJ, Burakiewicz J, Verschuuren JJ, Niks EH, Webb AG, Kan HE. Evaluation of skeletal muscle DTI in patients with duchenne muscular dystrophy. NMR Biomed. 2015; 28(11):1589–1597. [PubMed: 26449628]
74. Williams S, Heemskerk A, Welch E, Damon B, Park J. The quantitative effects of inclusion of fat on muscle diffusion tensor MRI measurements. J Magn Reson Imaging. 2013; 38(5):1292–1297. [PubMed: 23418124]
75. Nagy Z, Weiskopf N. Efficient fat suppression by slice-selection gradient reversal in twice-refocused diffusion encoding. Magn Reson Med. 2008; 60(5):1256–1260. [PubMed: 18956422]
76. Hernando D, Karampinos DC, King KF, Haldar JP, Majumdar S, Georgiadis JG, Liang ZP. Removal of olefinic fat chemical shift artifact in diffusion MRI. Magn Reson Med. 2011; 65(3): 692–701. [PubMed: 21337402]
77. Burakiewicz, J., Hooijmans, M., Niks, E., Verschuuren, J., Andrew GWebb, A., Kan, H. Toronto, ON: Olefinic fat suppression in skeletal muscle DTI with combined 6- and 2-point Dixon 2015.
78. Burakiewicz J, Charles-Edwards GD, Goh V, Schaeffter T. Water-fat separation in diffusion-weighted EPI using an IDEAL approach with image navigator. Magnetic Resonance in Medicine. 2015; 73(3):964–972. [PubMed: 24723244]

Author Manuscript Author Manuscript Author Manuscript Author Manuscript

79. Jezzard P, Balaban RS. Correction for geometric distortion in echo planar images from B0 field variations. Magn Reson Med. 1995; 34(1):65–73. [PubMed: 7674900]
80. Li Y, Xu N, Fitzpatrick JM, Dawant BM. Geometric distortion correction for echo planar images using nonrigid registration with spatially varying scale. Magn Reson Imaging. 2008; 26(10):1388–1397. [PubMed: 18499382]
81. Bhushan C, Haldar JP, Joshi AA, Leahy RM. Correcting susceptibility-induced distortion in diffusion-weighted MRI using constrained nonrigid registration. 2012 Dec.:1–9. 3–6 2012.
82. Irfanoglu MO, Walker L, Sarlls J, Marenco S, Pierpaoli C. Effects of image distortions originating from susceptibility variations and concomitant fields on diffusion MRI tractography results. Neuroimage. 2012; 61(1):275–288. [PubMed: 22401760]
83. Andersson JL, Skare S, Ashburner J. How to correct susceptibility distortions in spin-echo echo-planar images: application to diffusion tensor imaging. Neuroimage. 2003; 20(2):870–888. [PubMed: 14568458]
84. Morgan PS, Bowtell RW, McIntyre DJ, Worthington BS. Correction of spatial distortion in EPI due to inhomogeneous static magnetic fields using the reversed gradient method. J Magn Reson Imaging. 2004; 19(4):499–507. [PubMed: 15065175]
85. Aja-Fernandez S, Niethammer M, Kubicki M, Shenton ME, Westin CF. Restoration of DWI data using a Rician LMMSE estimator. IEEE Trans Med Imaging. 2008; 27(10):1389–1403. [PubMed: 18815091]
86. Hiepe P, Herrmann KH, Gullmar D, Ros C, Siebert T, Blickhan R, Hahn K, Reichenbach JR. Fast low-angle shot diffusion tensor imaging with stimulated echo encoding in the muscle of rabbit shank. NMR Biomed. 2014; 27(2):146–157. [PubMed: 24151092]
87. Buck AKW, Ding Z, Elder CP, Towse TF, Damon BM. Anisotropic Smoothing Improves DT-MRI-Based Muscle Fiber Tractography. PloS one. 2015; 10(5):e0126953. [PubMed: 26010830]
88. Ding Z, Gore JC, Anderson AW. Reduction of noise in diffusion tensor images using anisotropic smoothing. Magn Reson Med. 2005; 53(2):485–490. [PubMed: 15678537]
89. Haldar JP, Wedeen VJ, Nezamzadeh M, Dai G, Weiner MW, Schuff N, Liang ZP. Improved diffusion imaging through SNR-enhancing joint reconstruction. Magn Reson Med. 2013; 69(1): 277–289. [PubMed: 22392528]
90. Lam F, Babacan SD, Haldar JP, Weiner MW, Schuff N, Liang ZP. Denoising diffusion-weighted magnitude MR images using rank and edge constraints. Magn Reson Med. 2014; 71(3):1272–1284. [PubMed: 23568755]
91. Van Hecke W, Leemans A, De Backer S, Jeurissen B, Parizel PM, Sijbers J. Comparing isotropic and anisotropic smoothing for voxel-based DTI analyses: A simulation study. Hum Brain Mapp. 2010; 31(1):98–114. [PubMed: 19593775]
92. Sinha S, Sinha U. Reproducibility analysis of diffusion tensor indices and fiber architecture of human calf muscles in vivo at 1.5 Tesla in neutral and plantarflexed ankle positions at rest. J Magn Reson Imaging. 2011; 34(1):107–119. [PubMed: 21608064]
93. Sinha U, Sinha S, Hodgson JA, Edgerton RV. Human soleus muscle architecture at different ankle joint angles from magnetic resonance diffusion tensor imaging. J Appl Physiol. 2011; 110(3):807–819. [PubMed: 21164150]
94. Levin DI, Gilles B, Madler B, Pai DK. Extracting skeletal muscle fiber fields from noisy diffusion tensor data. Med Image Anal. 2011; 15(3):340–353. [PubMed: 21345716]
95. Leemans A, Jones DK. The b-matrix must be rotated when correcting for subject motion in DTI data. Magn Reson Med. 2009; 61:1336–1349. [PubMed: 19319973]
96. Pierpaoli, C. Artifacts in diffusion MRI. In: Jones, DK., editor. Diffusion MRI. New York, NY: Oxford University Press; 2010. p. 784
97. Koay CG, Chang LC, Carew JD, Pierpaoli C, Basser PJ. A unifying theoretical and algorithmic framework for least squares methods of estimation in diffusion tensor imaging. J Magn Reson. 2006; 182(1):115–125. [PubMed: 16828568]
98. Koay CG, Carew JD, Alexander AL, Basser PJ, Meyerand ME. Investigation of anomalous estimates of tensor-derived quantities in diffusion tensor imaging. Magn Reson Med. 2006; 55(4): 930–936. [PubMed: 16526013]

Author Manuscript Author Manuscript Author Manuscript Author Manuscript

99. Veraart J, Sijbers J, Sunaert S, Leemans A, Jeurissen B. Weighted linear least squares estimation of diffusion MRI parameters: strengths, limitations, and pitfalls. Neuroimage. 2013; 81:335–346. [PubMed: 23684865]
100. Chang LC, Walker L, Pierpaoli C. Informed RESTORE: A method for robust estimation of diffusion tensor from low redundancy datasets in the presence of physiological noise artifacts. Magn Reson Med. 2012; 68(5):1654–1663. [PubMed: 22287298]
101. Tax CM, Otte WM, Viergever MA, Dijkhuizen RM, Leemans A. REKINDLE: robust extraction of kurtosis INDices with linear estimation. Magn Reson Med. 2015; 73(2):794–808. [PubMed: 24687400]
102. Friman O, Farneback G, Westin CF. A Bayesian approach for stochastic white matter tractography. IEEE Trans Med Imaging. 2006; 25(8):965–978. [PubMed: 16894991]
103. Koch MA, Norris DG, Hund-Georgiadis M. An investigation of functional and anatomical connectivity using magnetic resonance imaging. Neuroimage. 2002; 16(1):241–250. [PubMed: 11969331]
104. Hua K, Zhang J, Wakana S, Jiang H, Li X, Reich DS, Calabresi PA, Pekar JJ, van Zijl PC, Mori S. Tract probability maps in stereotaxic spaces: analyses of white matter anatomy and tract-specific quantification. Neuroimage. 2008; 39(1):336–347. [PubMed: 17931890]
105. Descoteaux M, Deriche R, Knosche TR, Anwander A. Deterministic and probabilistic tractography based on complex fibre orientation distributions. IEEE Trans Med Imaging. 2009; 28(2):269–286. [PubMed: 19188114]
106. Ciccarelli O, Behrens TE, Altmann DR, Orrell RW, Howard RS, Johansen-Berg H, Miller DH, Matthews PM, Thompson AJ. Probabilistic diffusion tractography: a potential tool to assess the rate of disease progression in amyotrophic lateral sclerosis. Brain. 2006; 129(Pt 7):1859–1871. [PubMed: 16672290]
107. Kan JH, Heemskerk AM, Ding Z, Gregory A, Mencio G, Spindler K, Damon BM. DTI-based muscle fiber tracking of the quadriceps mechanism in lateral patellar dislocation. J Magn Reson Imaging. 2009; 29(3):663–670. [PubMed: 19243049]
108. Mori S, van Zijl PC. Fiber tracking: principles and strategies - a technical review. NMR Biomed. 2002; 15(7–8):468–480. [PubMed: 12489096]
109. Damon, BM., Ding, Z., Anderson, AW. Development of DT-MRI muscle fiber tracking algorithms. Toronto, ON Canada: 2008.
110. Froeling, M., Strijkers, G., Jeurissen, B., Paardt, M., van der Stoker, J., Nicolay, K., Nederveen, A., Leemans, A. Fiber architecture of the female pelvic floor: An exploratory investigation using different diffusion MRI tractography algorithms. Mentreal, QC Canada: 2011.
111. Li K, Dortch RD, Welch EB, Bryant ND, Buck AK, Towse TF, Gochberg DF, Does MD, Damon BM, Park JH. Multi-parametric MRI characterization of healthy human thigh muscles at 3.0 T - relaxation, magnetization transfer, fat/water, and diffusion tensor imaging. NMR Biomed. 2014; 27(9):1070–1084. [PubMed: 25066274]
112. Heemskerk AM, Sinha TK, Wilson KJ, Ding Z, Damon BM. Quantitative assessment of DTI-based muscle fiber tracking and optimal tracking parameters. Magn Reson Med. 2009; 61(2): 467–472. [PubMed: 19161166]
113. Damon BM, Heemskerk AM, Ding Z. Polynomial fitting of DT-MRI fiber tracts allows accurate estimation of muscle architectural parameters. Magn Reson Imaging. 2012; 30(5):589–600. [PubMed: 22503094]
114. Wakeling JM, Jackman M, Namburete AI. The effect of external compression on the mechanics of muscle contraction. J Appl Biomech. 2013; 29(3):360–364. [PubMed: 22927518]
115. Bolsterlee B, Veeger HEJ, van der Helm FCT, Gandevia SC, Herbert RD. Comparison of measurements of medial gastrocnemius architectural parameters from ultrasound and diffusion tensor images. Journal of Biomechanics. 48(6):1133–1140.
116. Heemskerk AM, Sinha TK, Wilson KJ, Ding Z, Damon BM. Repeatability of DTI-based skeletal muscle fiber tracking. NMR Biomed. 2010; 23(3):294–303. [PubMed: 20099372]
117. Damon BM, Ding Z, Anderson AW, Freyer AS, Gore JC. Validation of diffusion tensor MRI-based muscle fiber tracking. Magn Reson Med. 2002; 48(1):97–104. [PubMed: 12111936]
118. Mathworld, W. Curvature. Champaign, IL: 2011.

Author Manuscript Author Manuscript Author Manuscript Author Manuscript

119. Heemskerk AM, Strijkers GJ, Vilanova A, Drost MR, Nicolay K. Determination of mouse skeletal muscle architecture using three-dimensional diffusion tensor imaging. Magn Reson Med. 2005; 53(6):1333–1340. [PubMed: 15906281]
120. Okamoto Y, Kunimatsu A, Kono T, Kujiraoka Y, Sonobe J, Minami M. Gender differences in MR muscle tractography. Magn Reson Med Sci. 2010; 9(3):111–118. [PubMed: 20885084]
121. Budzik JF, Le Thuc V, Demondion X, Morel M, Chechin D, Cotten A. In vivo MR tractography of thigh muscles using diffusion imaging: initial results. Eur Radiol. 2007; 17(12):3079–3085. [PubMed: 17639406]
122. Kermarrec E, Budzik JF, Khalil C, Le Thuc V, Hancart-Destee C, Cotten A. In vivo diffusion tensor imaging and tractography of human thigh muscles in healthy subjects. AJR Am J Roentgenol. 2010; 195(5):W352–W356. [PubMed: 20966300]
123. Zijta F, Froeling M, van der Paardt M, Lakeman M, Bipat S, Montauban van Swijndregt A, Strijkers G, Nederveen A, Stoker J. Feasibility of diffusion tensor imaging (DTI) with fibre tractography of the normal female pelvic floor. Eur Radiol. 2011; 21(6):1243–1249. [PubMed: 21197534]
124. Shinagawa H, Murano EZ, Zhuo J, Landman B, Gullapalli RP, Prince JL, Stone M. Effect of oral appliances on genioglossus muscle tonicity seen with diffusion tensor imaging: a pilot study. Oral Surg Oral Med Oral Pathol Oral Radiol Endod. 2009; 107(3):e57–e63. [PubMed: 19217012]
125. Sinha U, Csapo R, Malis V, Xue Y, Sinha S. Age-related differences in diffusion tensor indices and fiber architecture in the medial and lateral gastrocnemius. Journal of Magnetic Resonance Imaging. 2015; 41(4):941–953. [PubMed: 24771672]
126. Maganaris CN, Baltzopoulos V, Ball D, Sargeant AJ. In vivo specific tension of human skeletal muscle. J Appl Physiol. 2001; 90(3):865–872. [PubMed: 11181594]
127. Heemskerk, AM., Damon, BM. DTI-based fiber tracking reveals a multifaceted alteration of pennation angle and fiber tract length upon muscle lengthening. Honolulu, HI: 2009.
128. Heemskerk, AM., Ding, Z., Sinha, TK., Wilson, KJ., Damon, BM. In vivo muscle fiber curvature measurements using DT-MRI. Montreal, QC, Canada: 2011.
129. Schwenzer NF, Steidle G, Martirosian P, Schraml C, Springer F, Claussen CD, Schick F. Diffusion tensor imaging of the human calf muscle: distinct changes in fractional anisotropy and mean diffusion due to passive muscle shortening and stretching. NMR in Biomedicine. 2009; 22(10):1047–1053. [PubMed: 19618408]
130. Felton SM, Gaige TA, Benner T, Wang R, Reese TG, Wedeen VJ, Gilbert RJ. Associating the mesoscale fiber organization of the tongue with local strain rate during swallowing. J Biomech. 2008; 41(8):1782–1789. [PubMed: 18456271]
131. Englund EK, Elder CP, Xu Q, Ding Z, Damon BM. Combined diffusion and strain tensor MRI reveals a heterogeneous, planar pattern of strain development during isometric muscle contraction. American Journal of Physiology - Regulatory, Integrative and Comparative Physiology. 2011; 300(5):R1079–R1090.
132. Levin, DIW., Gilles, B., Mädler, B., Pai, DK. MICCAI Workshop on Computational Diffusion MRI. New York, NY: 2008. A fiber tracking method for building patient specific dynamic musculoskeletal models from diffusion tensor data; p. 62-71.
133. Choe AS, Stepniewska I, Colvin DC, Ding Z, Anderson AW. Validation of diffusion tensor MRI in the central nervous system using light microscopy: quantitative comparison of fiber properties. NMR Biomed. 2012; 25(7):900–908. [PubMed: 22246940]
134. Gao Y, Choe AS, Stepniewska I, Li X, Avison MJ, Anderson AW. Validation of DTI tractography-based measures of primary motor area connectivity in the squirrel monkey brain. PloS one. 2013; 8(10):e75065. [PubMed: 24098365]
135. Schilling K, Janve V, Gao Y, Stepniewska I, Landman BA, Anderson AW. Comparison of 3D orientation distribution functions measured with confocal microscopy and diffusion MRI. Neuroimage. 2016; 129:185–197. [PubMed: 26804781]
136. Knosche TR, Anwander A, Liptrot M, Dyrby TB. Validation of tractography: Comparison with manganese tracing. Hum Brain Mapp. 2015; 36(10):4116–4134. [PubMed: 26178765]

Author Manuscript Author Manuscript Author Manuscript Author Manuscript

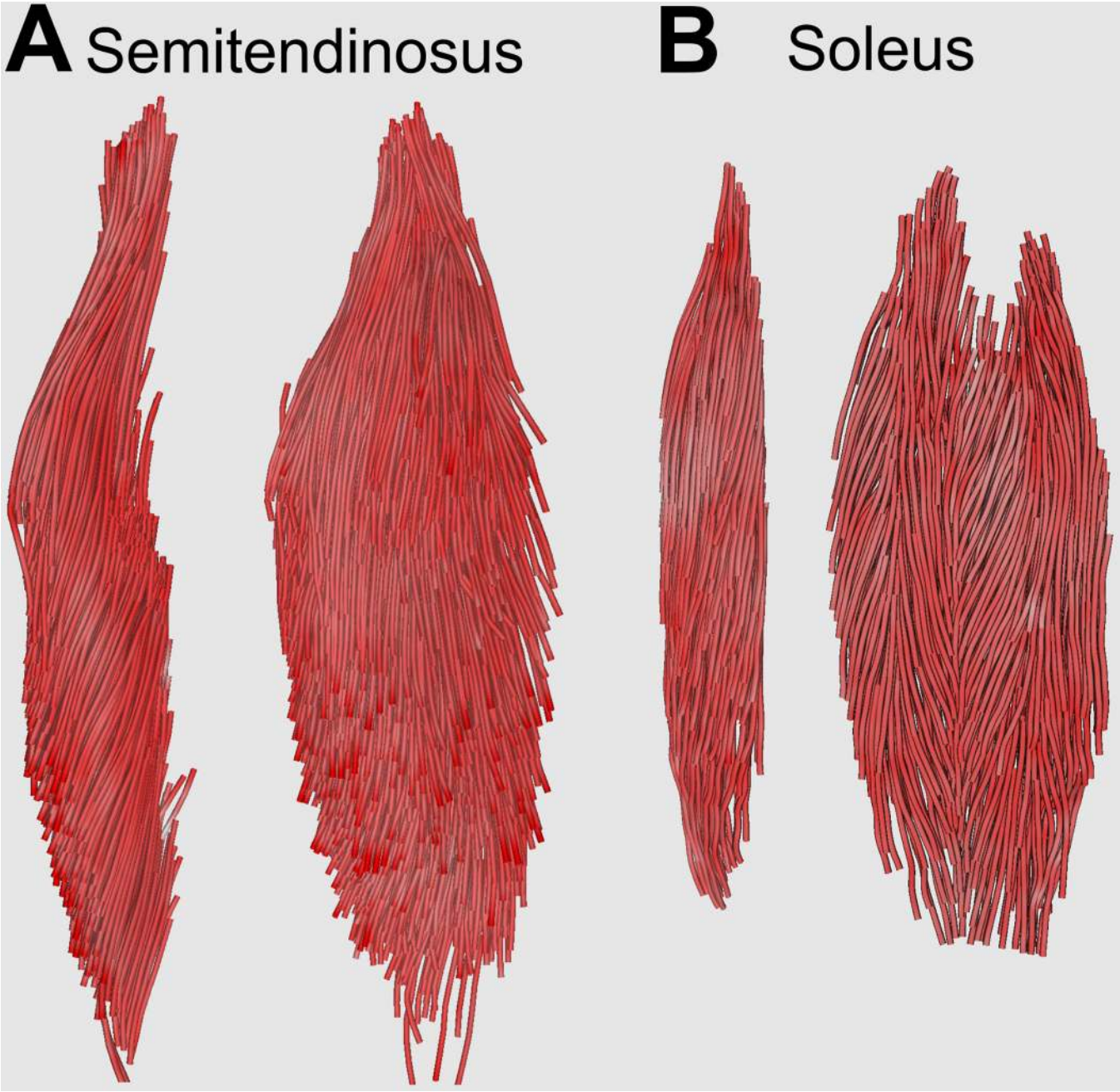

Figure 1.
Example fiber tracking of (A) fusiform muscle (semitendinosus) and (B) pennate muscle (soleus). A) Lateral and posterior view of the semitendinosus which shows its long muscle fibers and substantial surface of the tendon of insertion. B) Lateral and anterior view of the soleus. The lateral view shows the long fibers of the posterior and marginal soleus, whereas the anterior view clearly shows the pennate structure of the anterior soleus.

Author Manuscript Author Manuscript Author Manuscript Author Manuscript

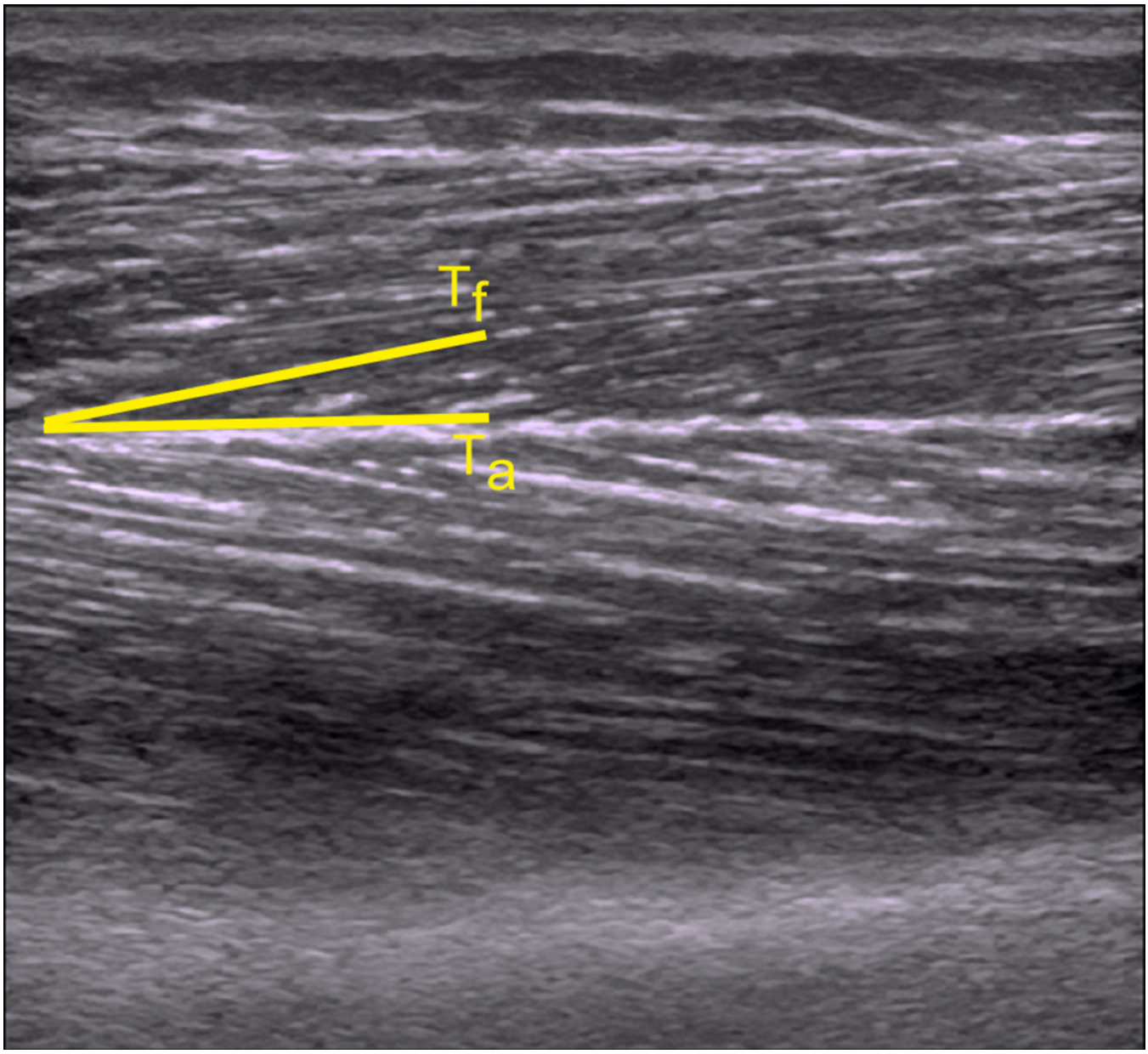

Figure 2.

B-mode ultrasound image of the tibialis anterior muscle. The top margin of the image displays the skin and subcutaneous fat overlying the anterior compartment of the leg. Deep to this, the tibialis anterior muscle is shown. A bipennate structure is noted, with a superficial compartment and a deep compartment. The high signal structure separating the compartments is the aponeurosis, or central tendon into which the fibers insert. The tangent line T_a indicates its orientation, while the tangent line T_f indicates the local fascicle orientation. The angle between these lines is θ.

Author Manuscript Author Manuscript Author Manuscript Author Manuscript

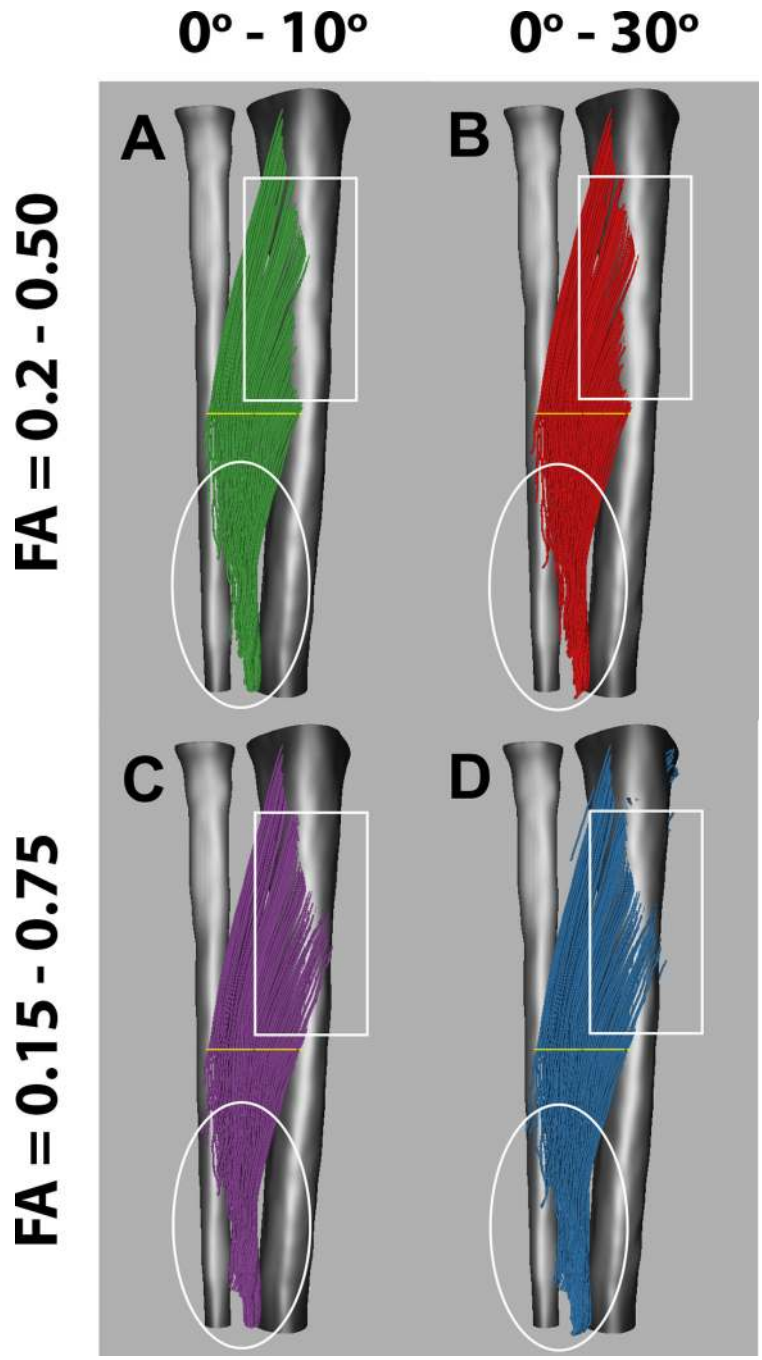

Figure 3.

Fiber tracking of the tibialis anterior muscle using different fiber tracking stopping criteria. (A, C) Allowed angle change of 0° – 10° per fiber tracking step. (B, D) Allowed angle change of 0° – 30° per fiber tracking step. (A, B) Allowed FA range of 0.20 – 0.50. (C, D) Allowed FA range of 0.15 – 0.75. The different stopping criteria affect the length of the fibers, the apparent tendon insertion points, and the amount of spurious fibers (as primarily observed in the areas enclosed by the white boxes and ellipses), whereas the muscle belly appears similar for different tracking parameters.

Author Manuscript Author Manuscript Author Manuscript Author Manuscript

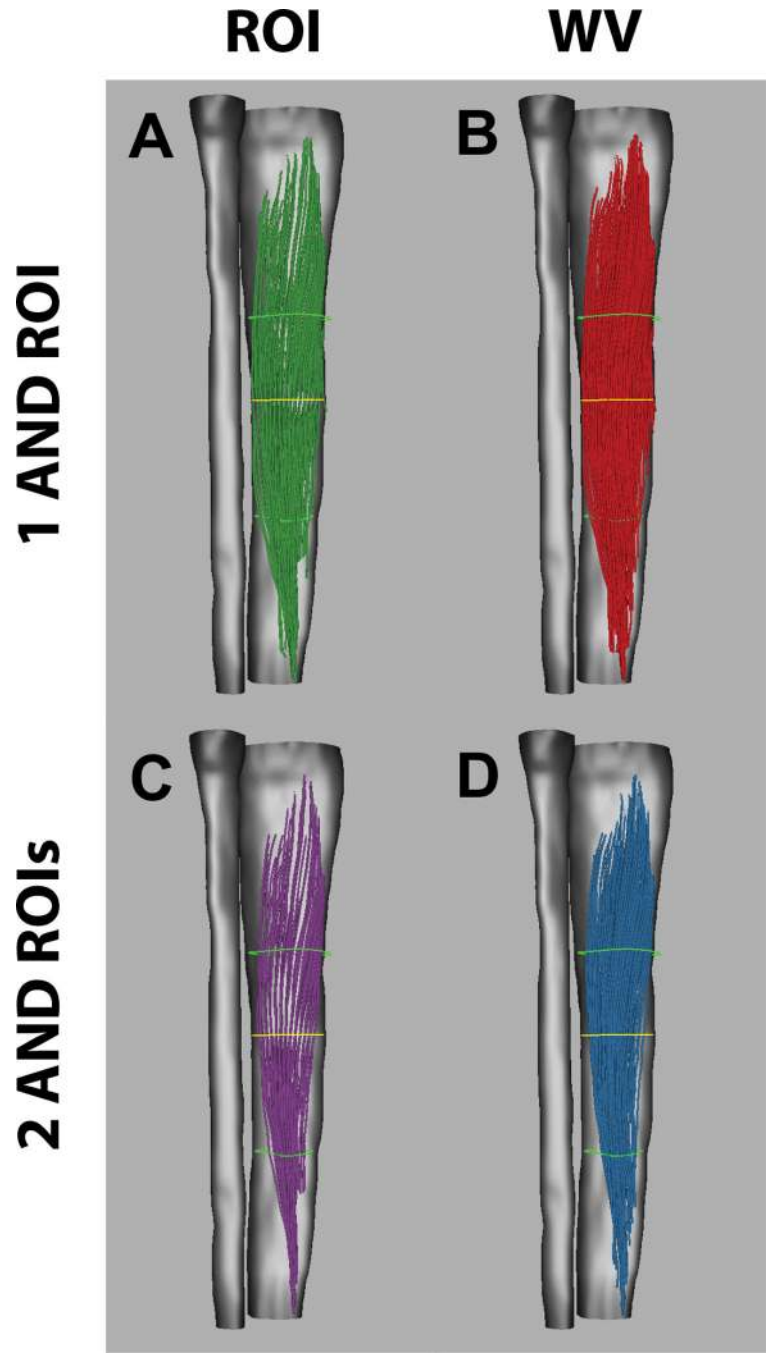

Figure 4.

Illustration of different fiber tracking seeding methods. (A, C) Fiber tracking is seeded from the yellow region of interest. (B, D) Fiber tracts are seeded in the whole muscle volume (WV). Only those fibers which cross the yellow region of interest are visualized. Whole volume seeding results in denser more homogeneous fiber tracking throughout the whole tibialis anterior muscle. (C, D) Fiber tracking results can be further refined by adding one or more AND (or NOT) ROIs shown in green. Only those fibers that cross both green regions of interest are visualized.

Author Manuscript Author Manuscript Author Manuscript Author Manuscript

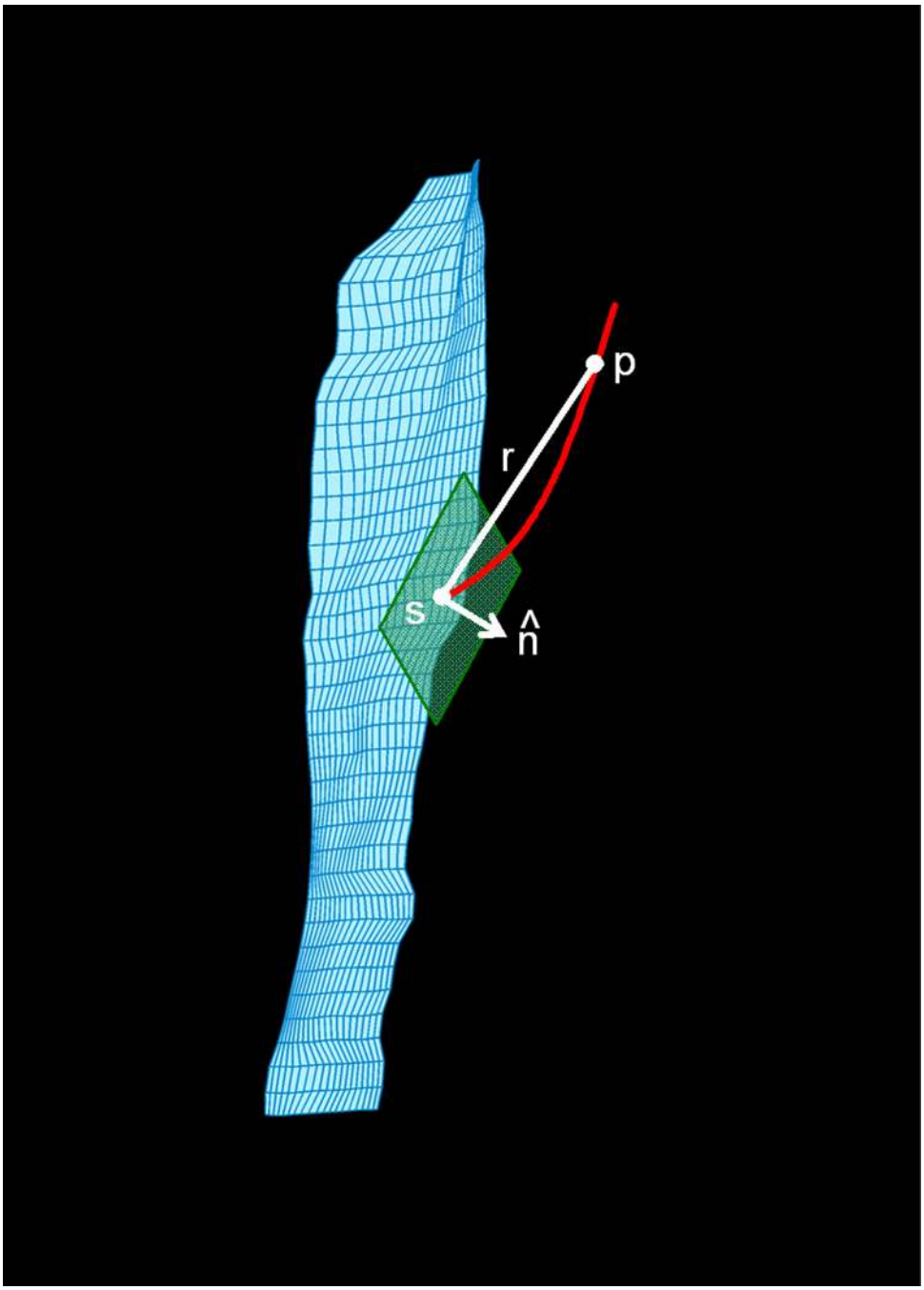

Figure 5.

Illustration of method for calculating the pennation angle. The green plane indicates the plane lying tangent to the seed point s, from which a fiber tract emerges (red curved line). The white lines indicate the direction vector **r** and the normal unit vector n̂ This figure was previously published (52) and is used with permission of the *Journal of Applied Physiology*.